Geothermics 127 (2025) 103255

Contents lists available at ScienceDirect

Geothermics

journal homepage: www.elsevier.com/locate/geothermics

Applications and implications of monitoring surface hydrothermal deposits at Lastarria Volcano, Chile, using multispectral satellite data and cloud computing

Guosheng Gao [a,*], Thomas R. Walter [a,b], Daniel Müller [a], Pouria Marzban [a,b,c], Simon Plank [d]

[a] GFZ Helmholtz Centre for Geosciences, Telegrafenberg, Potsdam, Germany
[b] Institute of Earth and Environmental Sciences, University of Potsdam, Potsdam, Germany
[c] German Archaeological Institute (DAI), Scientific Computing Unit, Central Research Services, Berlin, Germany
[d] German Remote Sensing Data Center (DFD), German Aerospace Center (DLR), Wessling, 82234, Germany

ARTICLE INFO

Keywords:
Hydrothermal alteration
Hydrothermal deposits
Google Earth Engine
Lastarria Volcano
Time series analysis

ABSTRACT

Studies of hydrothermal alteration involve the effects of circulating hot and aggressive fluids in volcanic environments, which are crucial for understanding volcanic hazards, slope instability, and steam-driven explosions. Visible hydrothermal deposits at the surface provide direct evidence of subsurface hydrothermal systems or volcanic unrest and can be detected by remote sensing tools. Here, we introduce the Hydrothermal Deposit Index (HDI), a remote sensing-based index derived from the Ultra Blue, Red, SWIR 1, and SWIR 2 bands of multispectral satellite data that allows spatiotemporal analysis of surface hydrothermal deposits. We apply the HDI approach to Lastarria, a stratovolcano on the border between Chile and Argentina that shows vigorous fumarole activity. With the support of Google Earth Engine (GEE), we mitigate environmental interferences like steam plumes and snow, thereby guaranteeing the precision of findings. Our HDI results identify three main depositional zones on the Lastarria Volcano, covering approximately 600,000 m^2, and are validated against independent field surveys. Time series analysis reveals three distinct patterns of HDI variation and dynamic shifts in hydrothermal activity within the summit crater and flank regions. Furthermore, we demonstrate that activity at the summit and flanks occurs in succession and that an increase in HDI concurs with the appearance of new sulphur flows. This research contributes to the advancement of remote sensing methodologies for volcano monitoring and emphasizes the importance of spatiotemporal dynamics in hazard assessment.

1. Introduction

Hydrothermal alteration involves the interaction between hydrothermal fluids and the ground, leading to a variety of changes in the host rock, such as oxidation, dissolution, replacement, and precipitation (Schwartz, 1959; Barrett and MacLean, 1997; Heap et al., 2021; Schaefer et al., 2023). These processes are fundamental to the study of volcanoes, enabling the identification of active fumaroles, potential failure areas and faults, and magmatic cooling (Darmawan et al., 2022; Kereszturi et al., 2023; Schaefer et al., 2023). For example, hydrothermal activity significantly affected the permeability and strength of the lava dome rocks at Mt. Merapi, leading to a shutdown of degassing prior to steam-driven explosions (Heap et al., 2019), while the weakening of rock contributes to the instability of volcanic edifices, resulting in hazards such as dome and flank collapse (Darmawan et al., 2022). Furthermore, increased hydrothermal activity has been observed preceding major volcanic eruption periods, as demonstrated by studies on the Usu Volcano (Africano and Bernard, 2000), Rincón de la Vieja (Montanaro et al., 2022) and Poás Volcano (Rodríguez and van Bergen, 2017). Investigations of active and hazardous volcanoes emphasize the importance of monitoring the spatiotemporal variations in hydrothermal alteration to improve our understanding of associated volcanism.

Typically, hydrothermal alteration affects volcanoes from the interior outward, making direct observation difficult. However, surface hydrothermal deposits can provide evidence and valuable insights into the understanding of these subsurface geological dynamics (John et al., 2008; Kereszturi et al., 2020; Müller et al., 2021; García-Soto et al., 2024). In particular, remote sensing techniques have become indispensable in such studies since they offer fast and effective methods for

* Corresponding author.
E-mail address: guosheng@gfz-potsdam.de (G. Gao).

https://doi.org/10.1016/j.geothermics.2025.103255
Received 31 July 2024; Received in revised form 8 December 2024; Accepted 6 January 2025
Available online 3 February 2025

geological mapping, including the identification of hydrothermal materials as well (Kereszturi et al., 2018; Mia et al., 2019). By comparing the captured spectral signatures of hydrothermally altered materials with existing spectral libraries, remote sensing tools can effectively separate altered rocks from the background (Chabrillat et al., 2019). For example, the visible and near-infrared bands (VNIR; 400–1000 nm) have been used to highlight the presence of iron-bearing minerals (Mia and Fujimitsu, 2012; Izawa et al., 2019); the shortwave infrared bands (SWIR; 1100–2500 nm) are effective in detecting minerals like clay, kaolinite, and alunite, as they present higher reflectance between wavelengths of 1550 nm and 1750 nm, and absorption occurs between 2080 nm and 2350 nm (Di Tommaso and Rubinstein, 2007; Mia and Fujimitsu, 2012; Shebl et al., 2023).

Hydrothermal and epithermal deposits have been extensively studied in regions such as mineral belts, with the goal of mapping the current conditions in areas where geological processes are relatively stable (Pour et al., 2013; Frutuoso et al., 2021). However, active volcanoes are characterized by frequent hydrothermal activity, which contributes to the formation of a wide range of deposits, influenced by fluctuations in temperature, pH, and pressure (Jakobsson and Moore, 1986; John et al., 2008; Salaün et al., 2011; Mathieu, 2018). To understand the development of hydrothermal deposits at active volcanoes, repeated and long-term monitoring of fumaroles and their surroundings is necessary to comprehend the dynamic processes that shape volcanic environments and the associated mineralization patterns. Previous studies have successfully mapped hydrothermal deposits in volcanic areas using close-range remote sensing tools (Azzarini et al., 2001; Müller et al., 2021; Marzban et al., 2023), but they have not taken into account extended periods ranging from years to decades.

Both spaceborne multispectral and hyperspectral instruments offer valuable insights into the complex geological and hydrothermal deposit dynamics of volcanic regions. These technologies enable detailed analysis of mineral composition, surface temperatures, and volcanic gas emissions, improving our understanding of volcanic activity and its impact (Plank et al., 2020; Walter et al., 2022; Shevchenko et al., 2024). However, the practical application of hyperspectral data remains limited due to issues such as data availability and high band similarity (Gersman et al., 2008; Kereszturi et al., 2018, 2020). Fortunately, spaceborne multispectral satellite data have provided stable coverage and the necessary revisit intervals since the mid-eighties of the last century, making them ideal for long-term monitoring. For example, the NASA/USGS Landsat program has provided the largest and longest continuous satellite record of multispectral data. These data have been extensively utilized in various applications, including time series analysis for burned area monitoring (Roy et al., 2019), crop type mapping (Blickensdörfer et al., 2022), and grassland fractional vegetation cover assessment (Okujeni et al., 2024). Additionally, recent advancements such as the ESA Copernicus Sentinel 2 multispectral satellite have further expanded these data streams, offering promising opportunities for long-term monitoring of volcanic systems (Massimetti et al., 2020).

The Google Earth Engine (GEE) platform currently provides access to both historical and current satellite data and supports high-performance computing tasks (Hird et al., 2017). In this study, we present a novel approach and application for spatiotemporal analysis of surface hydrothermal deposits by utilizing multispectral satellite data within the GEE cloud computing environment. Our study focuses on the Lastarria Volcano, located on the Chile-Argentina border, where frequent degassing always poses significant challenges for conducting time series analysis. However, studying this complex environment could provide valuable insights that increase the applicability of our methodology to similar volcanic regions worldwide. The primary objectives are to determine the extent of surface hydrothermal deposits and their spatiotemporal evolution patterns. This will be achieved by detecting e.g., hydroxyl-bearing minerals, iron oxide, and native sulphur, which are major components of hydrothermal alteration products and significantly influence volcano stability (Heap et al., 2021; Darmawan et al., 2022). In addition, we also discuss the implications at the Lastarria Volcano, such as the unrest in 2019 including two newly developed sulphur flows (Inostroza et al., 2023). We critically discuss the performance of the new Hydrothermal Deposit Index (HDI), created based on the Ultra Blue, Red, SWIR 1, and SWIR 2 bands, and elaborate on its strengths and weaknesses. Landsat 8 data are primarily utilized due to their longer temporal coverage, while data from Sentinel 2 and Pleiades satellites serve as supplementary sources. Overall, the methodology used in this study has successfully identified surface hydrothermal deposit information and could be applied to similar environments.

2. Study area and methodology

2.1. Study area

Lastarria Volcano (25.168°S, 68.507°W) is located on the border between Chile and Argentina in the Central Andean Volcanic Zone (see Fig. 1A). The discovery of a $> 1000\ km^2$ uplift in the Lazufre volcanic area has brought intense scientific and public attention to Lastarria Volcano, which lies on the northern margin of the Lazufre uplift region (Pritchard and Simons, 2002). Although no historical eruption has been recorded, Lastarria Volcano is characterized by strong degassing and ground displacements attributed to a shallow source less than 1 km deep (Froger et al., 2007; Ruch et al., 2009), as well as underlying hydrothermal reservoirs reported in previous studies (Spica et al., 2015). Notably, a large area of intense gas emissions, abundant fumaroles, and hydrothermal deposits characterized by pale yellow sulphur and sulphate deposits have been found within the summit crater, along the NW flank, and on the eastern and western edges of the summit rim (Fig. 1B and 1C). The hydrothermal minerals belong mainly to seven families, including sulphate, hydrated sulphate, sulphides, halides, carbonates, silicates, and native element sulphur (Aguilera et al., 2016). Although recent studies have shown deceleration in uplift at the Lastarria volcanic centre (Henderson et al., 2017), the discovery of new sulphur flows in 2019 is likely related to the possible reactivation of magma or hydrothermal systems (Inostroza et al., 2023). Furthermore, the aridity and acidity of the environment mean that vegetation is scarce, making the land surface very homogeneous and ideal for remote sensing studies.

2.2. Data

GEE has been widely used for accessing and processing Earth Observation (EO) data (Gorelick et al., 2017). This platform provides online access to archived surface reflectance products, including Landsat and Sentinel 2 satellite data. The atmospherically corrected Landsat 8 Level 2, Collection 2, Tier 1 surface reflectance products from 2014 to 2023, specifically, Path 233 and Row 077, were primarily used in the analysis, as we found it best covered the study area. For the ~10-year interval considered, images from May to September were excluded due to snow accumulation effects, as the elevation of the Lastarria reaches approximately 5700 m above sea level (a.s.l.). Harmonized Sentinel 2 Level 2 surface reflectance products, covering the period October to April each year from 2018 to 2023, were used for validation. Two georeferenced Pleiades satellite images, one from 2016 and the other from 2022, were used for visual analysis, both images have a resolution of 0.5 m in the panchromatic band and 2 m in the multispectral bands. Detailed information on the satellite images used can be found in Table 1.

2.3. Methodology

The schematic framework, illustrated in Fig. 2, offers an overview of the methodology employed in this study. First, we define the input dataset, which includes Landsat 8 and Sentinel 2 satellite data accessed through the GEE platform. We then outline the data processing steps employed to study hydrothermal deposits across the study area. Finally, we integrate Pleiades data and field observations into the analysis.

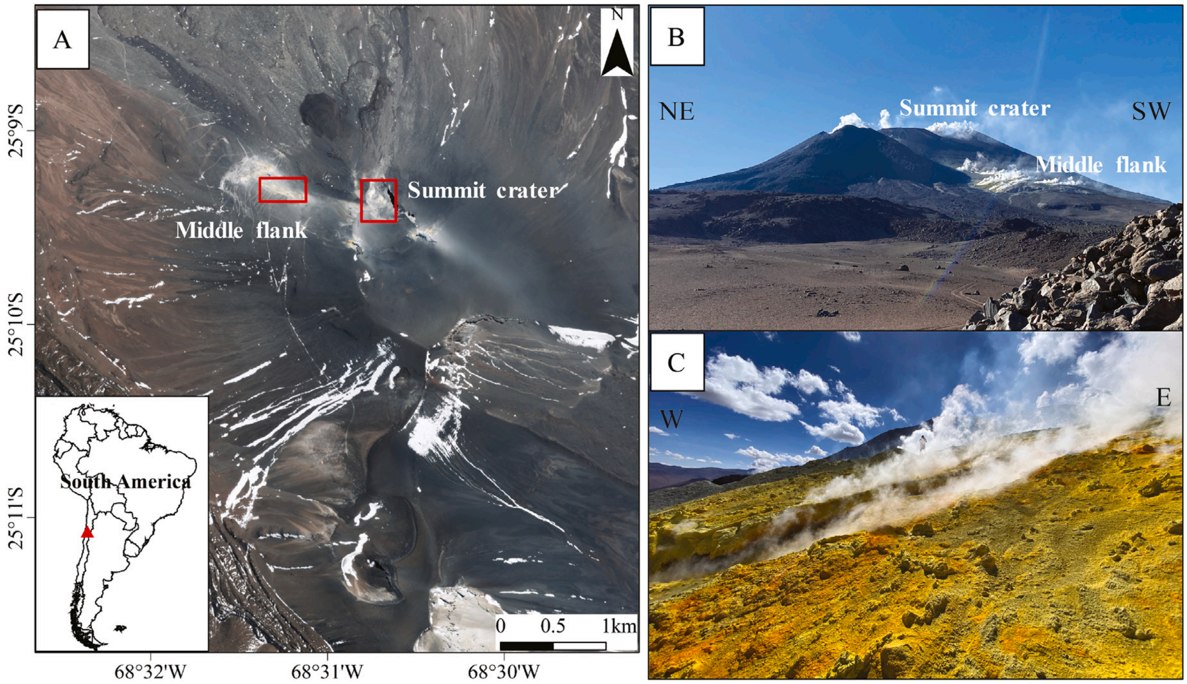

Fig. 1. (A) Satellite view of Lastarria Volcano from the Pleiades image acquired in 2022. White patches indicate snow, while dark textures represent lava flows, and brownish-grey areas correspond to pyroclastic and redeposited materials. Red rectangles mark the locations of alteration near the summit crater and middle flank, which are the main focus areas of this study; (B) Photograph showing the NW flank of Lastarria and locations of the fumaroles on the middle flank and summit; (C) Photograph showing the sulphur-rich hydrothermal deposits on the NW flank of Lastarria. (For interpretation of the references to colour in this figure legend, the reader is referred to the web version of this article.)

Table 1
Data sources and band information: Landsat 8, Sentinel-2 (GEE), and Pleiades.

Satellite	Band name	Description	Wavelength centre	Resolution
Landsat 8	SR_B1	Ultra Blue	443 nm	30 m
	SR_B4	Red	655 nm	30 m
	SR_B6	SWIR 1	1609 nm	30 m
	SR_B7	SWIR 2	2201 nm	30 m
Sentinel 2	B1	Ultra Blue	443.9 nm (S2A)/442.3 nm (S2B)	60 m
	B4	Red	664.5 nm (S2A)/665 nm (S2B)	10 m
	B11	SWIR 1	1613.7 nm (S2A)/1610.4 nm (S2B)	20 m
	B12	SWIR 2	2202.4 nm (S2A)/2185.7 nm (S2B)	20 m
Pleiades	–	Panchromatic	480-800 nm	0.5 m
	B0, B1, B2	Multispectral	450-700 nm	2 m

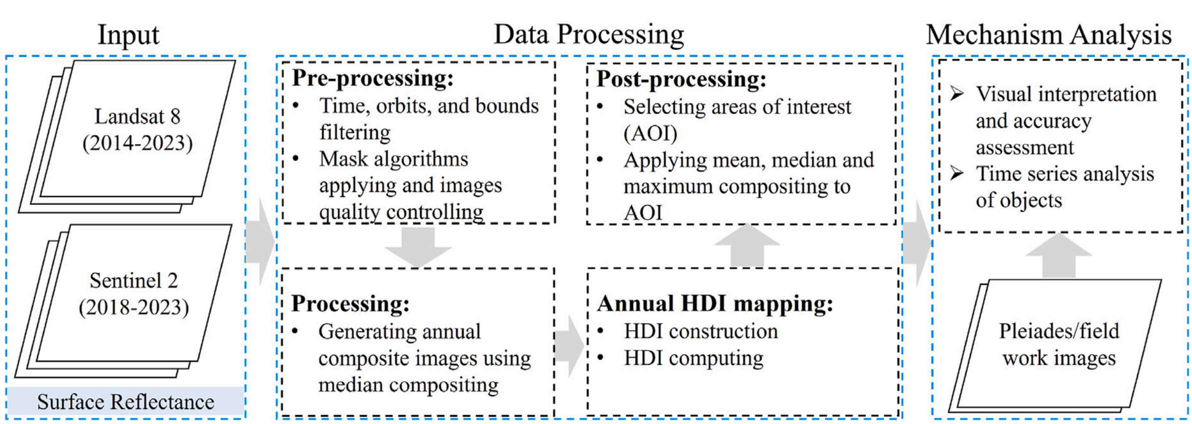

Fig. 2. Conceptual scheme of the surface hydrothermal deposit monitoring in this study.

2.3.1. HDI construction theory

Multispectral satellite data offers a robust tool for analysing specific surface features and compositional variations through techniques like band ratios and colour composites. These techniques enhance the information content that may not be apparent in individual bands and help reduce artefacts and environmental factors such as clouds, snow, and shadows, thereby improving analysis accuracy and reliability (Di Tommaso and Rubinstein, 2007; Mia et al., 2019). For example, the band ratio (6/7) of Landsat 7 has been used to detect clay minerals, whereas the ratio (4/2) can be employed to assess iron oxide minerals, they are key minerals of hydrothermally altered minerals and replacement products in the volcano (Aguilera et al., 2016; Abass Saley et al., 2021; Shebl et al., 2023). In addition to band ratios, statistical methods have demonstrated effectiveness, notably the Crosta method, which employs Principal Component Analysis (PCA) to emphasize spectral variations associated with specific minerals (Crósta and Moore, 1989; Mia et al., 2019). For example, the Crosta method has successfully identified alteration zones on the Lastarria Volcano by combining the Blue, Red, SWIR 1, and SWIR 2 bands of Landsat 7 (Aguilera et al., 2016). However, despite their practical utility, these approaches still face challenges from environmental conditions, and band ratios can occasionally yield extreme values (Thomas et al., 1987; AghaKouchak et al., 2015). Importantly, these methods are inadequate for conducting comprehensive time series analyses. The index, such as the Normalized Difference Vegetation Index (NDVI) has been successfully used to indicate vegetation greenness, with values ranging from −1 to 1, reflecting the degree of disturbance to densely vegetated areas (Defries and Townshend, 1994; Carlson and Ripley, 1997; Martínez and Gilabert, 2009; Li et al., 2021). This also provides a means of tracking the growth and health of vegetation, allowing for temporal and spatial comparisons (Myneni et al., 1997). Inspired by the success of the NDVI, here we extend upon these studies to introduce a novel semi-quantitative measure known as the Hydrothermal Deposit Index (HDI). We note that there have been previous attempts to develop a geochemical hydrothermal index, including the Alteration Index (AI) (Ishikawa et al., 1976), Chemical Index of Alteration (CIA) (Nesbitt and Young, 1982), Weathering Index of Parkar (WIP) (Parker, 1970), Loss on Ignition (LOI) (Lechler and Desilets, 1987), and Sulphur Index (Mathieu, 2018; García-Soto et al., 2024), each offering unique insights but also limitations. These are all based on in situ and laboratory analysis, meaning that there is as yet no widely applicable remotely sensed index.

Fieldwork and previous studies have shown that hydrothermal deposits in Lastarria Volcano are primarily composed of hydroxyl-bearing minerals such as hydrothermal clays, sulphates, and iron oxides (Aguilera et al., 2016). Fig. 3 shows the spectral reflectance curves of primary indicators for these hydrothermally altered rocks, derived from laboratory analyses. Native sulphur is abundant throughout the volcanic region, while alunite and kaolinite serve as key indicators for hydroxyl-bearing minerals, and goethite and jarosite are essential markers for iron oxides. These key indicators exhibit higher reflectance in the Red and SWIR 1 bands of Landsat 8 (Fig. 3A), with distinct absorption occurring in the SWIR 2 band (Fig. 3B). For this reason, these three bands have been widely utilized for mineral classification (Sun et al., 2017; Sengar et al., 2020). In contrast, background elements such as cinders, clouds, water, and snow have a lower reflectance in the two SWIR bands or a slightly higher reflectance in SWIR 1 than in SWIR 2, as shown in Fig. 3A. In addition, we performed a pixel-by-pixel examination of the spectral reflectance characteristics in the alteration zones, which largely align with our analysis as mentioned above based on the spectral library. Therefore, we first used the ratio (SWIR 1 - SWIR 2)/(SIWR 1 + SWIR 2) to identify the hydrothermal alteration zone. Based on this, the larger positive values could be related to altered materials, whereas negative values could indicate interferences. However, the differences in reflectance and absorption features between hydrothermal deposits and background materials are less distinct in the SWIR 1 and SWIR 2 bands compared to the NIR and Red bands typically used for NDVI analysis, as shown in Fig. 3. This implies that distinguishing between minerals and background materials may be challenging due to the smaller spectral differences, as discussed further in the following chapter. Moreover, interferences such as vegetation also tend to have a higher reflectance in SWIR 1 and a lower reflectance in SWIR 2, potentially complicating the identification of hydrothermal alteration. To address this, we introduce an Hydrothermal Deposit Index (HDI) incorporating a coefficient specifically tailored for the time series analysis of hydrothermal deposits, as detailed below:

$$HDI = \left(\frac{\text{Red}}{\text{Ultra Blue}}\right) \times \left(\frac{\text{SWIR 1} - \text{SWIR 2}}{\text{SWIR 1} + \text{SWIR 2}}\right) \tag{1}$$

where Red, Ultra Blue, SWIR 1, and SWIR 2 are multispectral bands. This adjustment is because the atmospherically corrected Ultra Blue band is often employed to track phytoplankton in coastal and inland waters (Olmanson et al., 2016; Hafeez et al., 2022). Under clear and dry atmospheric conditions, the reflectance of the Ultra Blue band remains consistently low and stable, as elaborated in the Discussion section. For the Red band, altered materials typically have a higher reflectance, while interferences such as vegetation, which have historically confused mineral classification, generally show a lower reflectance (see Fig. 3A). In particular, the differences in reflectance of interference between the Red and Ultra Blue bands can be minimal or even contradictory. In the past, although the Red/Ultra Blue band ratio has been less utilized in mineral detection due to the limited availability of satellites equipped with the Ultra Blue band, the Red/Blue ratio has been widely employed in minerals monitoring like iron oxides (Frutuoso et al., 2021; Shebl et al., 2023). Therefore, after multiplication, the HDI values of altered materials are largely greater than the interferences, and the proposed HDI is useful in identifying hydrothermal deposits related to both hydroxyl-bearing minerals and iron oxides.

2.3.2. *Data processing and analysis workflow*

In order to determine the extent of hydrothermally altered materials and perform a time series analysis, data processing involves three steps, primarily executed within the GEE platform, as shown in Fig. 2.

Step 1: Data pre-processing involves filtering and masking of Landsat 8 and Sentinel 2 imagery. For the Lastarria case study, a 30% cloud cover threshold was applied during the selection of satellite imagery, and only images captured between October and April were selected to minimize snow cover effects. Then, the CFMask algorithm (Zhu and Woodcock, 2014), integrated into the Landsat “QA_PIXEL” band in GEE, was further used to mask residual clouds, cloud shadows, cirrus clouds, and snow in Landsat 8 imagery. Sentinel 2 imagery was masked using the QA60 bitmask band in GEE. Previous studies have demonstrated the effectiveness of these masking bands in cloud-related studies (Carrasco et al., 2019; Bian et al., 2020), and this study even confirmed their capability to reduce the impact of steam plumes. Following these procedures, a total of 278 images were processed for the period 2014–2023, consisting of 11 to 14 Landsat 8 and 2 to 41 Sentinel 2 images per year, respectively (Table 2). It should be noted, Sentinel 2 images, fulfilling the aforementioned cloud threshold condition, are not available between 2014 and 2017. The two high-resolution Pleiades images were georeferenced and registered for comparison.

Step 2: Generating annual composite images and calculating HDI. Environmental factors have always been a challenge for remote sensing applications, especially in volcanic environments where frequent and dense steam plumes are prevalent. Although we applied the masking calculation in the first step, it is still challenging to ensure that all relevant interferences, particularly thin clouds, steam plumes, and snow, are fully removed. In this study, we addressed this by creating annual composite images, including RGB and HDI composites. In GEE, the EE.Reducer algorithm provides minimum, mean, median, and maximum filters, allowing for easy compositing of data across time, space, bands, arrays, and various other data structures (Gorelick et al., 2017). Compared with other filters, the median filter is more robust in hydrothermal alteration studies. This is because environmental influences, such as seasonal variations in vegetation and changes in the presence and direction of steam plumes across images, are variable. In contrast, rock alteration even in volcanic regions, progresses slowly and is characterized by stable absorption and emission characteristics. This means that persistent and consistent changes in HDI values over the long-term may suggest anomalies in magmatic or hydrothermal systems, whereas temporary and abrupt fluctuations are likely to be

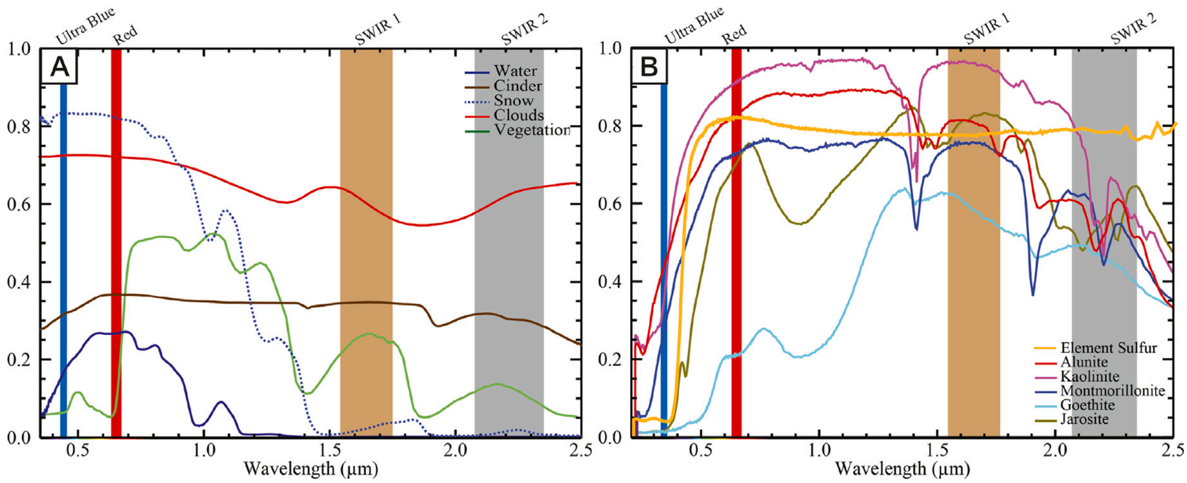

Fig. 3. Selected spectral reflectance curves for background interferences (A) and hydrothermally altered minerals (B), visualized from the USGS spectral library in ENVI software (NV5 Geospatial Solutions). The four vertical bars of Ultra Blue, Red, SWIR 1, and SWIR 2 bands correspond to Landsat 8 channels (cf. Table 1). (For interpretation of the references to colour in this figure legend, the reader is referred to the web version of this article.)

Table 2
The number of images included in this study from 2014 to 2023.

	2014	2015	2016	2017	2018	2019	2020	2021	2022	2023
Landsat 8	13	12	11	13	13	13	13	13	11	14
Sentinel 2	–	–	–	–	2	20	25	19	41	38
Pleiades	–	–	1	–	–	–	–	–	1	–

due to disturbances. Therefore, median compositing with a substantial number of high-quality images could effectively reduce the variability related to interference, thereby enhancing visualization and denoising non-stationary signals. The results will demonstrate in Section 3 that annual composites are less affected by environmental factors.

Step 3: Post-processing and data analysis. This step primarily involves integrating multi-source remote sensing data to interpret and analyse hydrothermal deposits, including Landsat 8, Sentinel 2, and Pleiades satellite data. First, we evaluated the quality of the annual composites by performing a visual analysis to assess the removal of clouds, snow, cloud shadows, and steam plumes. Then, we assessed the accuracy of the HDI in the surface hydrothermal deposit mapping and compared it with field observations and previous studies. Subsequently, the study area was divided into several smaller subregions for detailed time series analysis. Within these subregions, the mean, median, and maximum HDI values were all calculated, ensuring the correctness of the acquired time series analysis.

3. Results

3.1. The identification of hydrothermal deposits

The effectiveness of the masking bands and the annual median compositing approach in reducing disturbances and emphasizing targets are demonstrated first. Using the Landsat 8 image acquired on 17 March 2021 as an example (Fig. S1A), we compared the performance of the unmasked (Fig. S1B) and masked (Fig. S1C) images. The masking band effectively eliminate poor-quality pixels and highlight regions of interest. The improvement is particularly noticeable at fumarole sites, where persistent steam plumes indicated by the blue ellipse are masked (Fig. S1B). Furthermore, Figs. S1C and S1D offer a clearer comparison between the 2021 intra-year median composite image and the individual masked image, demonstrating that the composite image has higher pixel quality, fewer gap areas, and reduced residual noise. Other Landsat 8 annual composites from 2014 to 2023 are shown in Fig. S2, with similar positive outcomes (the analysed GeoTIFF raster files can be downloaded from https://doi.org/10.5281/zenodo.10893855). These findings underscore the significant potential of reducing background noise and utilizing annual composite images in the subsequent analysis.

Using Landsat 8 annual composite imagery, we generated hydrothermal deposit images from 2014 to 2023, with HDI values ranging from 0.6 (warmer colours, highly altered) to 0 (colder colour, unaltered), as shown in Fig. S3. Based on our field observations, the HDI value of 0.17 can be used as a threshold to effectively discriminate between unaltered and altered materials. Using the 2017 Landsat 8 HDI scenario as an example (Fig. 4), the hydrothermal deposit zones at Lastarria Volcano can be identified in three main parts: (i) The NW slope of the volcano (Fig. 4B), where the map view reveals an elongated NW-SE trending area that expands on its NW side to form a "T"-shape zone of hydrothermal deposits. The HDI values tend to be higher (above 0.5) in the two extension zones of this "T"-shape, but lower along the slope (mostly below 0.2); (ii) Summit crater area (Fig. 4C): Higher HDI values are concentrated around the four active fumaroles, with most values above 0.3. The maximum HDI values are consistently found on the western rim (above 0.6). In addition, the area (red ellipse in Fig. 4C) has relatively higher values despite having few active fumaroles. Another region to the north of the main summit crater (white ellipse in Fig. 4A) shows a linear distribution of median HDI values; (iii) The southern zone hosts hydrothermal deposits that display moderate HDI values, with no significant active fumarole. Its distribution has shown minimal change in both the time and space domains, suggesting the absence of new vent formation or fumarole activity. Overall, the identified hydrothermal deposit extent by HDI on Lastarria is consistent with our field observation, with an area of approximately 600,000 m^2. Visual analysis based on annual HDI images indicates the minor spatial variation in the period from 2014 to 2023 (Fig. S3).

3.2. Application of HDI for long-term monitoring of hydrothermal deposits

Although visual analysis have indicated that the spatial extent of hydrothermal deposits remain relatively stable from 2014 to 2023 (Fig. S3), long-term monitoring of pixel-level HDI values can provide insight into local hydrothermal activity. Thus, we selected the summit crater

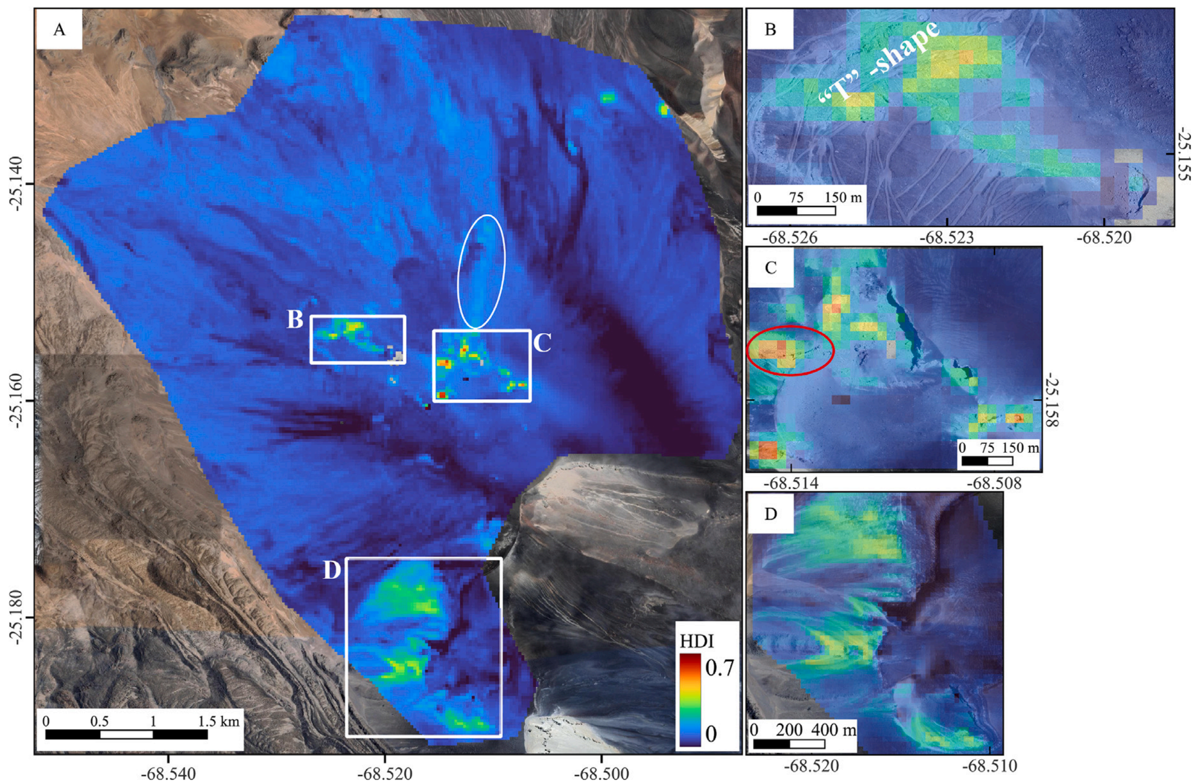

Fig. 4. (A) 2017 Landsat 8 HDI results, manually cropped to focus on key areas, show HDI values ranging from low (colder colour) to high-intensity hydrothermal deposits (warmer colour). Panels B, C, and D show enlarged views of the rectangles B (flank), C (summit crater), and D (slopes in the south) in Panel A, respectively, using the same colour bar as in Panel A and set to 50% transparency. The red and white ellipses indicate HDI anomaly areas, see text for details. (For interpretation of the references to colour in this figure legend, the reader is referred to the web version of this article.)

area and the middle flank as new study area subsets (see Fig. 1). Two sulphur flows have been reported on the middle flank (Inostroza et al., 2023), while significant changes in alteration areas in the summit crater can be observed from the high-resolution data (Fig. S4). Due to limited resolution and minimal change, other zones have not been included. In this chapter, the time series analysis was mainly based on Landsat 8 HDI imagery, with Pleiades and Sentinel 2 used as auxiliary data for validation. In most subareas, the mean, median, and maximum HDI values were all calculated to ensure the accuracy and reliability of the time series results. In addition, different reference areas were also selected within each subregion to evaluate the influence of environmental factors.

3.2.1. The summit crater area

The summit crater was further divided into three hydrothermal deposit subareas: A1, A2, and A3, with A0 serving as the reference area (Fig. 5A). The time series results for A0 exhibit a stable condition without much variation (Fig. 5D), with HDI values (mean, median, and max) varying only between 0.12 and 0.15 (below the threshold of 0.17), indicating successful filtering of environmental influences in long-term analysis and the absence of hydrothermal deposits. Nevertheless, slight fluctuations in HDI values in 2018 may still be environmentally influenced, potentially affecting A1, A2, and A3 as well. A1 mainly consists of two active fumaroles and has exhibited long-term degassing, as observed in our fieldwork. The time series analysis indicates stability in the mean, median, and max HDI values from 2014 to 2016, followed by a notable decline in 2017 (Fig. 5E). Subsequently, the HDI values stabilize once again from 2018 to 2023 but remain lower than in the previous period (Fig. 5E). A2 presents similar trendline variations, especially HDI variation in 2017 (Fig. 5F). In these two subareas, the HDI values are between 0.25 and 0.5 (above the defined threshold), indicating the presence of highly altered materials. The decline in HDI observed in 2017 suggests a decrease in the area of surface hydrothermal deposits. As shwon in Fig. 5B-C and S4, there is a slight colour shift at the junction of A1 and A2. In A3, evident growth of deposit zones can be observed from satellite images (Fig. 5A-C and S4). Although the precise onset remains uncertain, historical imagery suggests the expansion likely started after 2011 and ended before 2019, as shown in Fig. S4. While our HDI time series results show an uptrend from 2014 to 2017, peaking at around 0.7 on the maximum trend line in 2018 (Fig. 5G). If the HDI values from 2018 are recognized as outliers following the results of the time series analysis conducted on A0, this implies that the period from 2018 to 2023 exhibits a stable trend. These findings align with historical imagery, showing little change after 2019, but growth observed after 2014. (Fig. S4).

3.2.2. The middle flank area

In the middle flank, we focus mainly on the two newly developed sulphur flows, which we refer to as the upper and lower sulphur flows respectively, along with their surrounding regions (Fig. 6B). Although the exact start and end times of these two sulphur flows remain unknown, it has been suggested that they were initiated or at least active around 2019 (Inostroza et al., 2023). As the sulphur flows (B1 and B3 in Fig. 6B) are covered by only one Landsat 8 pixel, the median HDI values are equal to the mean and maximum values. Meanwhile, we also calculated only the median HDI value for B4 to avoid confusion. As shown in Fig. 6E, the trend line for the reference area (B0) exhibits instability from 2014 to 2023, with HDI values generally between 0.08 and 0.09, aside from an outlier in 2018. This outlier aligns with what has been observed in the summit crater. For the lower sulphur flow, B1 is used to indicate its location, while B2 shows its point of origin (Fig. 6B). Before 2019, the HDI values in B1 remain stable and below the defined threshold, indicating that there were limited hydrothermal deposits or only slight alteration. Following about three years of HDI

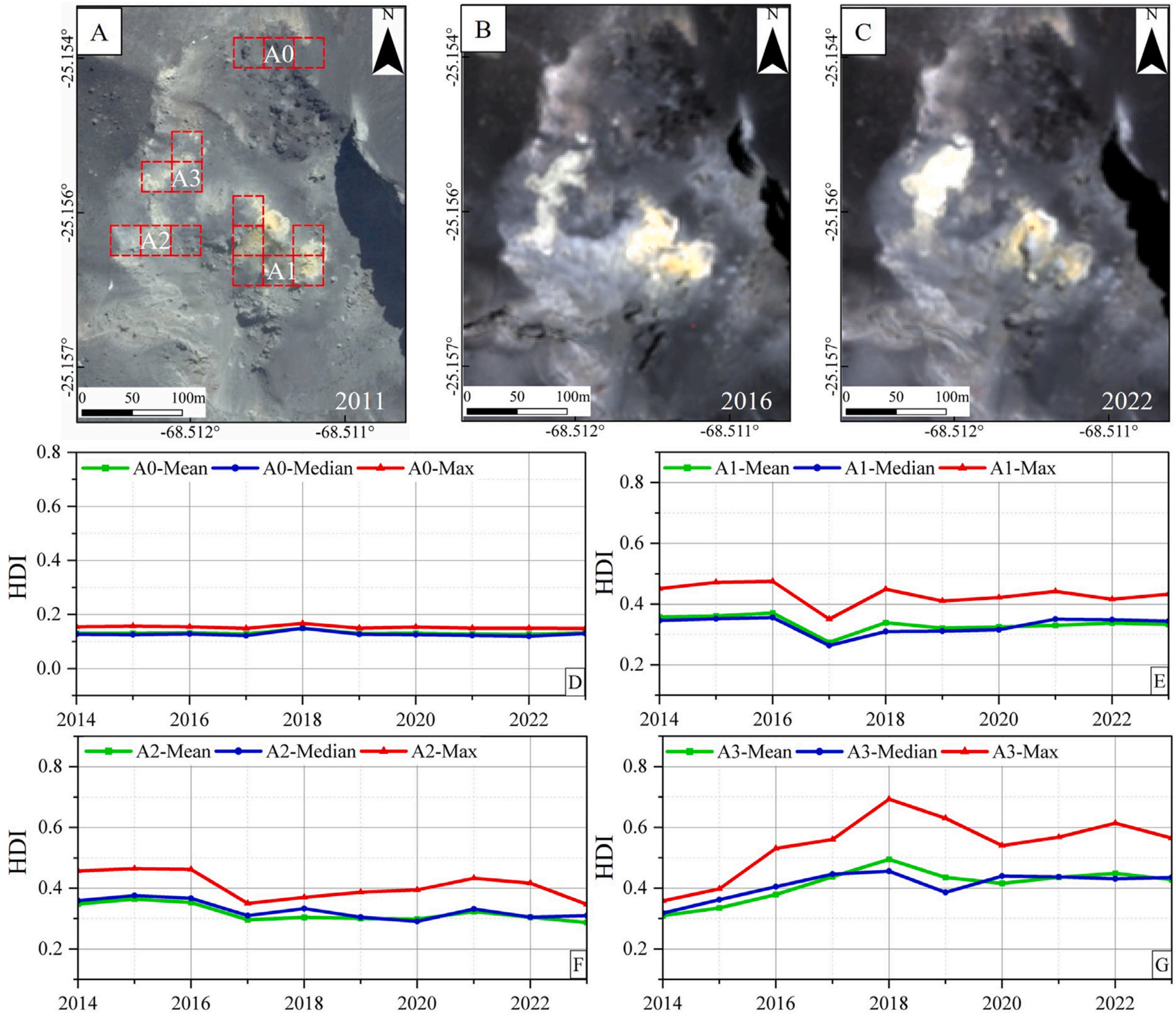

Fig. 5. Landsat 8 HDI results in the Lastarria summit area. The map views show the summit area in different years, from the Vivid imagery in 2011 (A), and the Pleiades imagery in 2016 (B) and 2022 (C), respectively. The four HDI time series plots (D)–(G) correspond to four subregions (A0 to A3), which are indicated by red squares in (A). These squares illustrate the specific pixel locations used for Landsat 8 HDI analysis within subareas. Subregions A1, A2, and A3 correspond to zones of hydrothermal deposition, while A0 serves as a reference area. The mean, median, and maximum values represent the HDI measurements across the subareas. (For interpretation of the references to colour in this figure legend, the reader is referred to the web version of this article.)

increase, a decline is observed after 2021. The HDI values in B2 are consistently higher than those in B1, remaining above the threshold from 2014 to 2023, and B2 exhibits a greater rate of increase from 2018 to 2020. Additionally, the increase in B2 occurs earlier than in B1, which begins in 2018. The upper sulphur flow (B3) exhibits stable variations in HDI values from 2014 to 2017 and is consistently above the defined threshold (Fig. 6D). Following an increase starting in 2018 and peaking at 0.25 in 2020, HDI values in B3 then decline from 2021 to 2023. Similarly, the HDI variations within B3 are smaller compared to those observed in its source area, B4. In addition, the HDI values in the flank area are overall lower than those observed in the summit crater, both in reference areas and targets.

3.3. Comparisons of Landsat 8 and Sentinel 2 HDI results

Our study represents a pioneering effort in long-term monitoring of surface hydrothermal deposits, where establishing reliability is essential. To address this, we investigated several satellite sources. Landsat 7 was excluded due to SLC-off artefacts and changes in revisit times from 2019 to 2023 (Zeng et al., 2013), while Landsat 9 was limited by its narrower temporal coverage (Masek et al., 2020). Consequently, Sentinel 2 emerged as the preferred option for validation, despite the differences in band resolution. The improved resolution of the Red, SWIR 1, and SWIR 2 bands in Sentinel 2 provides more reliable detection of fine-scale hydrothermal deposits, but the lower resolution of the Ultral Blue band (60 m) and the limited number of Sentinel 2 images available in 2018 should be noted. Considering the significant variability and high confidence levels, we focus on HDI results in (i) the new sulphur flows on the middle flank and (ii) the summit crater area (Fig. 7A, 7C, and 7E), and only median values have been calculated for each new subarea. In 2018, the Sentinel 2 HDI value in the lower sulphur flow area (P1) is close to the reference, followed by a significant increase from 2019 to 2020 and a subsequent decrease from 2021 to 2023 (Fig. 7B). Comparatively, HDI variations in P2 follow similar patterns to those in P1, consistently showing significantly higher values and larger magnitudes across both the Landsat 8 and Sentinel 2 datasets (Fig. 7B). While the stable variation at the reference point demonstrates the effectiveness of the time series analysis for both P1 and P2. For the reference (P4) in the upper sulphur flow area (Fig. 7D), a notably higher HDI value is evident in 2018, similar to Landsat 8 (Fig. 6E). However, the upward trend observed in P3 and P4 from 2018 to 2020, followed by a decline from 2021 to 2023, seems reasonable (Fig. 7D). Furthermore, the HDI values around the main fumaroles surrounding the sulphur flow are consistently higher than those within the sulphur flow

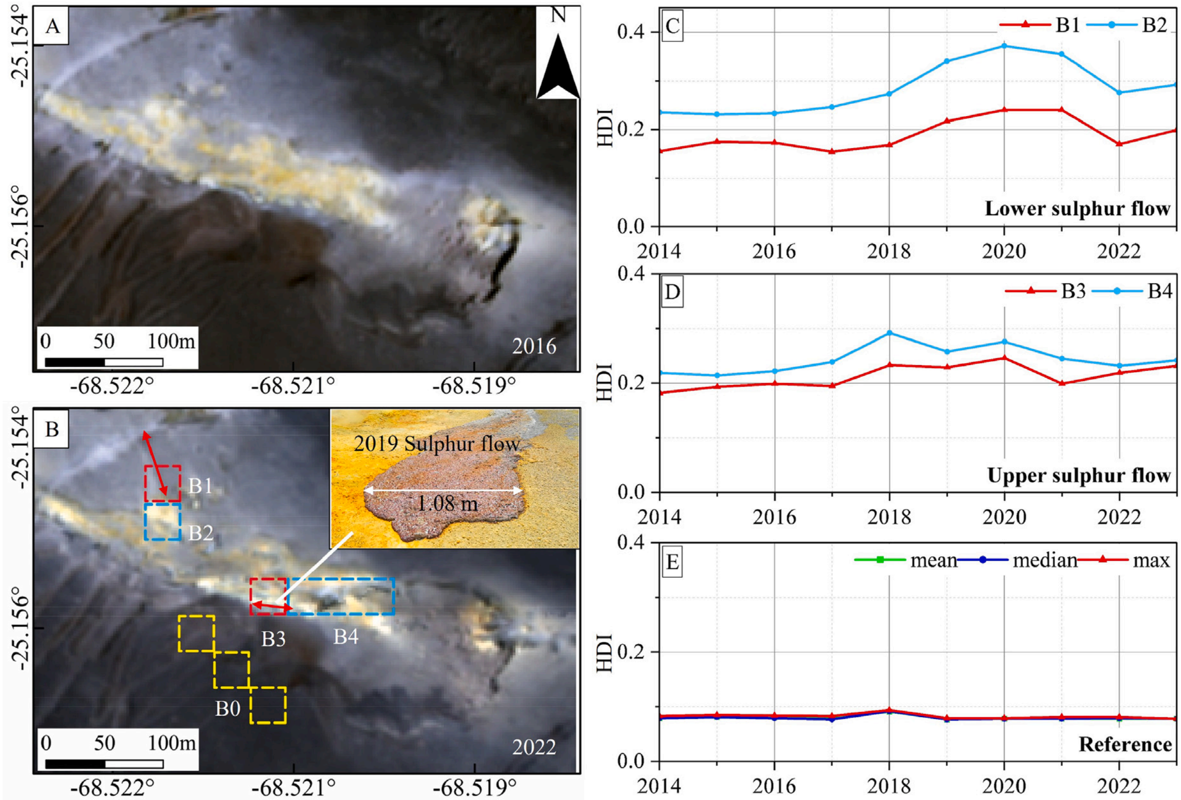

Fig. 6. Landsat 8 HDI monitoring results in the Lastarria middle flank area, divided into four subareas: B0 serves as the reference area; B1 and B3 are sulphur flow areas, while B2 and B4 are origins of these two sulphur flows. The HDI time series plots (C)–(E) correspond to five subregions (B0 to B4), which are indicated by squares in (B). These squares illustrate the specific pixel locations used for Landsat 8 HDI analysis within these subareas. The background images are from the Pleiades satellite in 2016 and 2022, respectively; the red double-headed arrows indicate the locations of sulphur flows. Photograph of the sulphur flow from January 2019 showing its dimensions (see also Inostroza et al., 2023). The mean, median, and maximum values represent the HDI measurements in the reference area. (For interpretation of the references to colour in this figure legend, the reader is referred to the web version of this article.)

itself, consistent with the patterns observed in the lower sulphur flow. However, the presence of a larger area of surrounding hydrothermal deposits prevents the precise separation of the upper sulphur flow. In addition, the HDI results from Sentinel 2 reveal a significant increase in P3 and P4 in 2020. This discrepancy can be attributed to the pixel range difference between B4 in Fig. 6C and P4 in Fig. 7B. This observation may indicate an expansion of the hydrothermal deposit zone following the occurrence of the sulphur flow, as the observed dimensions (see Fig. 6) exceed those associated with the sulphur flow itself. In the summit crater area, Sentinel 2 HDI results exhibit a subtle upward trend from 2018 to 2023, but the outliers in 2021 and 2022 disrupt a clear and consistent trajectory over the entire period (Fig. 7F). Despite these challenges, our analysis provides robust validation, the observed HDI trends are consistent across the Landsat 8 and Sentinel 2 datasets, reinforcing the reliability of our findings.

3.4. Analysis and validation

The results were geospatially analysed using QGIS and ENVI, which are powerful tools for spatial data processing and visualization. First of all, we validated our HDI findings with field observations, including temperature measurements, gas emissions, and geochemical and mineralogical assessments. This empirical validation is essential to verify the performance and accuracy of remote sensing analysis. Subsequently, we compared our findings with band ratio results, which have been widely employed for the qualitative detection of hydrothermally altered mineral assemblies (Sabins, 1999; Ranjbar et al., 2004; Carrino et al., 2015). As illustrated in Fig. 8, the band ratio results were derived from a cloud-free Landsat 8 OLI image acquired on 13 February 2021, using band ratios of 6/7 for hydrothermal clay and 4/2 for iron oxides, which are prominent components at Lastarria (Aguilera et al., 2016). The extent identified by this traditional method, particularly band ratios 6/7, corresponds well with our HDI results (Fig. 8C). However, a more detailed analysis in the NW flank region reveals different higher-value pixel distributions (see areas 1, 2, and 3 in Fig. 8D, 8E, and 8F). This discrepancy arises because band ratios, such as 6/7, fail to adequately capture the extensive presence of natural sulphur and iron oxides throughout the Lastarria region. In addition, the hydrothermal clay area determined by the band ratio (6/7) exceeds the total alteration area identified in the field, while the iron oxide alteration area from the band ratio (4/2) is smaller than that observed in the field. On the contrary, our HDI results not only represent a combination of both minerals but also yield areas more consistent with field observations, as shown in Fig. 8F. Furthermore, the band ratio (6/7) shows a small difference between hydrothermal clay and the background, while the 4/2 ratio results in a background value exceeding that of the altered areas, posing a challenge for those without prior experience. Compared to traditional methods, our HDI results show a fivefold difference between the minimum and maximum values, offering a clearer distinction between altered and unaltered materials. This underscores the effectiveness of our approach for accurately mapping hydrothermally altered or deposited products, providing valuable insights into the spatial variability.

Furthermore, we also conducted a comparison between the results obtained without and with the inclusion of the coefficient in (Eq. (1)), where the coefficient refers to the calculation of Red/Ultra Blue. As

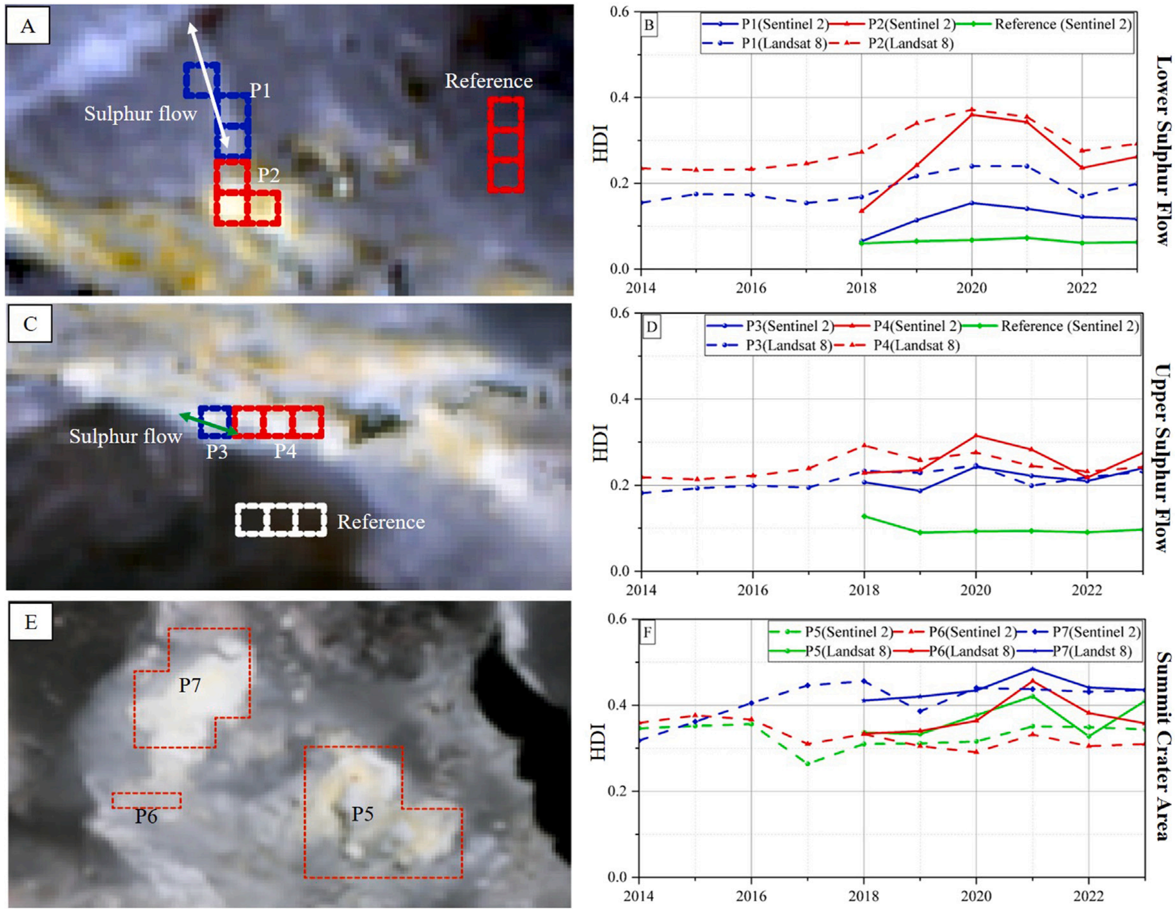

Fig. 7. Comparison of HDI monitoring results between Landsat 8 and Sentinel 2, with the background from Pleiades data acquired in 2022. The map views show the lower sulphur flow (A), upper sulphur flow (C), and summit crater (E), with squares highlighting the specific pixel locations used for Sentinel 2. (A) Pixel locations P1 and P2 represent the lower sulphur flow and the surrounding hydrothermal deposit zones, respectively; (C) Pixel locations P3 and P4 represent the upper sulphur flow and the surrounding hydrothermal deposit zones, respectively; (E) Pixel locations P5, P6, and P7 denote three hydrothermal deposit zones within the summit crater. Two references in panels A and C were selected from outside of fumaroles. Panels B, D, and F display the HDI time series results for both Landsat 8 and Sentinel 2. (For interpretation of the references to colour in this figure legend, the reader is referred to the web version of this article.)

shown in Fig. 9, highly altered materials are visualized by the proximity of colours to red, while pixels closer to blue generally indicate unaltered materials or interferences. Small gap areas correspond to the removed bad pixels, where a continuous gas plume has obscured the information at these pixels. The processing is based on the 2021 Landsat 8 median composite image covering the NW flank area. According to our experience, the values of 0.07 and 0.17 were set as the thresholds in scenarios without and with coefficient assignments, respectively. While both approaches demonstrate the capability to identify hydrothermal deposit zones, there are subtle differences that should be noted: (i) The scenario with the applied coefficient exhibits clearer distinctions and internal heterogeneities with surrounding feature types, especially in the middle area. This variability is also reflected in the mean, minimum, and maximum values in Table 3, where the two minimum HDI values are similar (around 0.02), but the maximum values differ significantly, with one being twice as high as the other at 0.231 and 0.512. (ii) Similar to band ratios, relying solely on two SWIR bands is insufficient for clearly separating altered materials from the background, particularly in the central part of Fig. 9A. While the differences between altered and unaltered are significant in Fig. 9B. (iii) Fig. 9B indicates a narrower range of hydrothermal deposit zones, as evidenced by the reduction in the proportion of above-threshold values from 46% to 32% (Table 3). This shift is related to different mineral assemblages and the influence of background has been reduced.

Table 3
Summary of statistics: Without vs. With inclusion of coefficient.

	Without coefficient		With coefficient	
	Below 0.07	Above 0.07	Below 0.17	Above 0.17
Mean	0.053	0.019	0.093	0.276
Proportion	54%	46%	68%	32%
Min	0.012		0.024	
Max	0.231		0.512	

4. Discussion

4.1. The performances and limits of individual bands

In this study, we have extracted information about surface hydrothermal deposit zones on Lastarria by combining multispectral bands, specifically Ultra Blue, Red, SWIR 1, and SWIR 2. To comprehensively assess our approach, we here evaluate the performances of these four distinct bands individually and compare them with HDI results based on the 2019 Landsat 8 intra-year median composite image. The surface reflectance of the Ultra Blue band, which has lower overall values compared to the other bands, is shown in Fig. 10A. Although relatively higher values were found at active fumaroles, Fig. S5 indicates that the reflectance of the Ultra Blue band remains stable in hydrothermal deposit zones over time. This means that utilizing

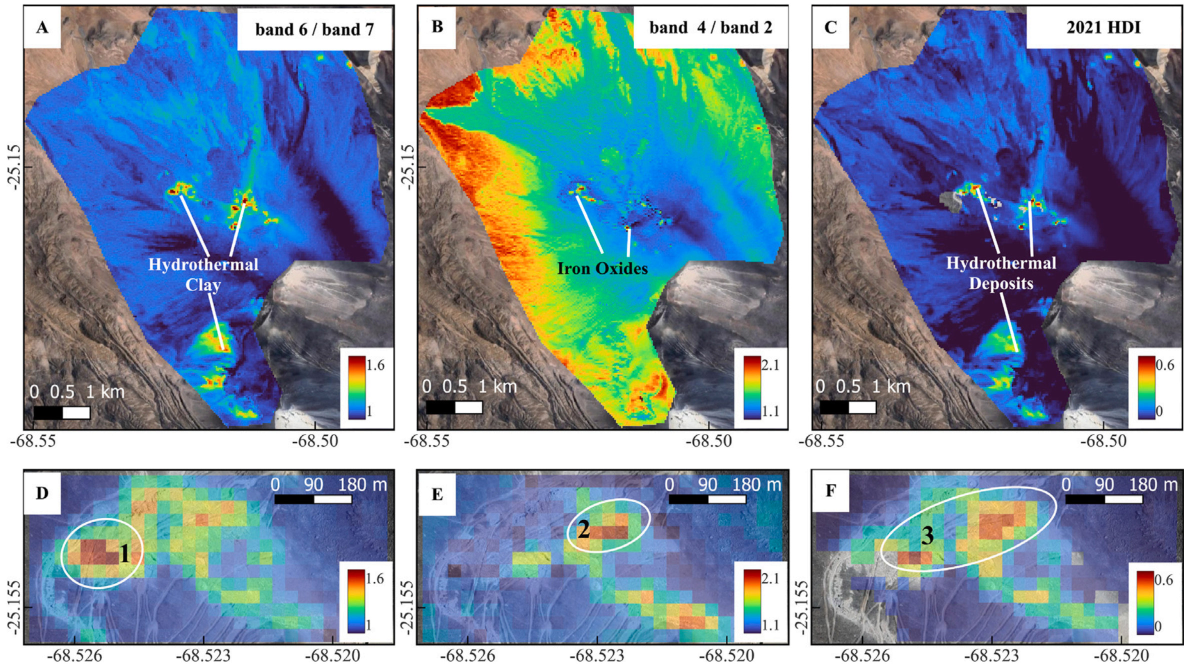

Fig. 8. The comparison between band ratios and HDI, with red tones indicating highly altered materials. (A) and (B) were derived from Landsat 8 OLI data captured on 13 February 2021, with (A) using the 6/7 band ratio for hydrothermal clay and (B) using the 4/2 band ratio for iron oxides. (C) shows the HDI results from the 2021 Landsat 8 annual composite image. Panels (D), (E), and (F) are enlarged views of the flank (cf. Fig. 4B), set to 50% transparency. The labels 1, 2, and 3 indicate the anomaly areas; see the text for details. (For interpretation of the references to colour in this figure legend, the reader is referred to the web version of this article.)

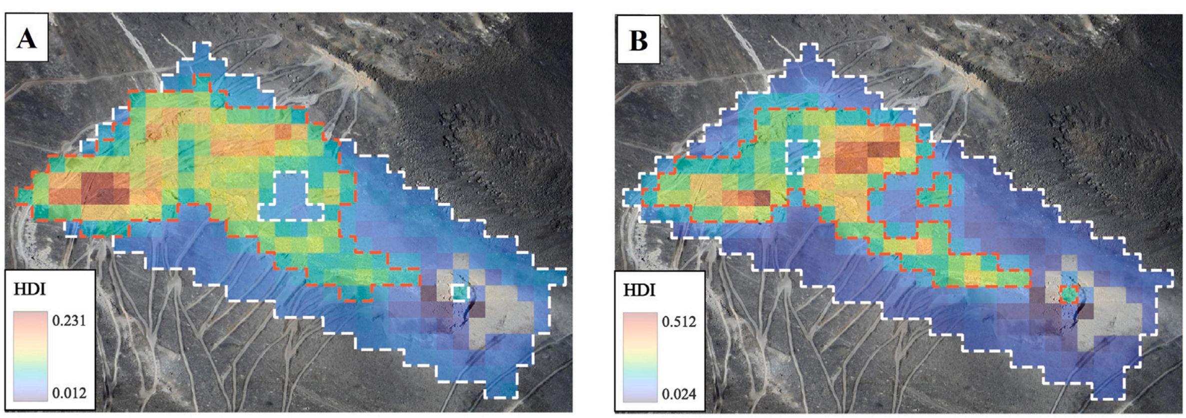

Fig. 9. Comparisons of the performance between without (A) and with (B) coefficient; the transparency was set to 50%. The red dashed lines represent the boundary between altered and unaltered materials, while the white dashed lines indicate the borders of the region of interest. (For interpretation of the references to colour in this figure legend, the reader is referred to the web version of this article.)

the Ultra Blue band as the denominator in our HDI computation could potentially enhance the sensitivity of other bands, while its own contribution and impact would be relatively small. However, two Ultra Blue peaks in 2019 and 2022 should be noted in Fig. S5. The 2019 Ultra Blue peak value is likely related to increased hydrothermal activity, leading to higher concentrations of water vapour, steam, or dust in the air. This finding is consistent with previous studies showing that the rate and concentration of gas emissions were indeed higher in 2019 (Lopez et al., 2018; Layana et al., 2023). Similarly, we consider that the 2022 Ultra Blue peak value is also associated with increased hydrothermal activity, although independent validation is lacking. For the Red band, higher reflectance is notable around the main fumarole sites and their surroundings, covering a larger area than the other three bands. However, both Ultra Blue and Red band could be significantly affected by snow, as indicated by the red ellipse in Fig. 10B and 10C. In contrast, SWIR 1 and SWIR 2 can effectively delineate hydrothermal deposits without being affected by snow, but they lack sensitivity to highlight highly altered materials in the summit area, as indicated by the black ellipse in Fig. 10H and 10I. Our HDI result not only ensures accurate delineation of hydrothermal deposits but also minimizes interference from factors like snow compared to individual bands (Fig. 10E). This is because the sign of the result is determined by the expression of (SWIR 1 - SWIR 2)/(SWIR 1 + SWIR 2) in the HDI computation (Eq. (1)), while the coefficient is used to highlight the presence of these altered products. The HDI values generally decrease as they extend outward from the central fumarole area, consistent with established patterns of hydrothermal deposits. Furthermore, our results are visually more significant in distinguishing between altered and unaltered materials compared to traditional methods such as Crosta PCA, LS-Fit, and band ratios in the previous study (Aguilera et al., 2016).

4.2. Hydrothermal deposits time series implications

Through HDI time series analysis, we have investigated the dynamics of hydrothermal deposits in both the summit crater and the

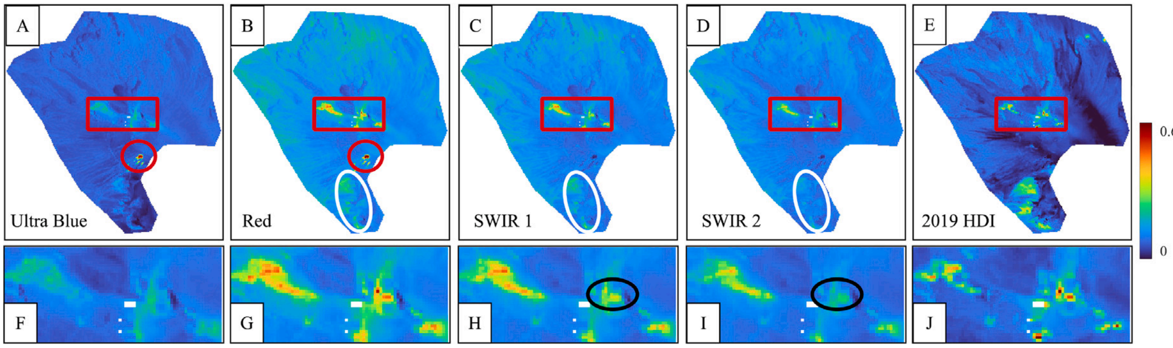

Fig. 10. Panels (A) to (E) show the surface reflectance for the Ultra Blue, Red, SWIR 1, and SWIR 2 bands, as well as the HDI result, respectively. All of these are derived from the 2019 Landsat 8 intra-year median composite image. The red, white, and black ellipses are areas of interest discussed in the main text. The second row shows zoomed-in views of the areas highlighted by red rectangles in the first row. (For interpretation of the references to colour in this figure legend, the reader is referred to the web version of this article.)

middle flank of the Lastarria. In the summit crater area, HDI values are consistently higher than those in the flank area, even when taking reference areas into account. This indicates that the primary mineral components in these two areas differ, as the HDI values in the summit crater are nearly twice those in the flank, as shown in Figs. 5 and 6. In the summit crater area, the hydrothermal deposit zones A1 and A2 are separate and not directly connected at the surface (Fig. 5A). However, we observed similar trends in HDI variation, which suggests that some fumarole zones are related and changes are concurring. In addition, A1 and A2 show a significant decrease that occurs almost simultaneously in 2017. Typically, this notable change is unlikely to be environmentally driven but rather triggered by specific events like land surface collapse or uplift. Meanwhile, the end time of the increase in the A3 and the sudden decrease in A1 and A2 occurred almost simultaneously (Fig. 5). We infer that geological structure changes may potentially influence local gas emission dynamics and hydrothermal activity, thereby preventing the escape of volcanic gases from A3. Therefore, our study reveals the potential of using this surface-based HDI to infer subsurface activity. Furthermore, contrasting observations in the flank area reveal heightened activity from 2018 to 2020, lagging behind those in the summit crater. Meanwhile, the magnitudes of HDI increase in the flank area are consistently lower than those in the summit crater. This could be explained by hydrothermal convection cells that are first feeding the volcano summit, and then diverging outwards to feed the flanks, as proposed by Aguilera and summarized in our conceptual model sketch (Fig. 11). According to previous studies, the permeability structure beneath Lastarria has a major effect on the pathways of fluids and surface expression (Aguilera et al., 2012; Layana et al., 2023). An area of high permeability is hypothesized beneath the summit craters and connects to the magmatic source at depth (Layana et al., 2023). This then diverges near the surface, and interacts with the groundwater and aquifer, to feed the flank fumarole fields (Aguilera et al., 2012). We conjecture that a higher permeability to the summit may explain the first onset of increased HDI there, which is followed by increases on the flanks where the permeability is lower and/or the fluid pathway is more complex (Fig. 11). This may be related to subsurface structural changes in 2017, which changed fluid flow pathways, potentially reflecting movements of subsurface magma or the migration of hydrothermal fluids from the summit crater to the flank area. The formation of sulphur flows could be related to the residual energy consumption resulting from fumarole expansion within the crater area. This assumption aligns with previous studies suggesting that increased inputs of hot magmatic fluids lead to the consumption of the hydrothermal system during this period (Lopez et al., 2018; Layana et al., 2023).

Based on HDI time series analysis, we also categorize the hydrothermal deposits at Lastarria Volcano into two types: (i) those associated with the dissolution and remineralization of the original rock mass, leading to hydrothermal deposit growth at the summit, and (ii) those linked to sulphuric deposits, which either precipitate from fumarole plumes or flow out at vents, forming sulphur flows on the flank. For the growth of surface hydrothermal deposits, HDI values increased for more than three years, followed by slight decreases. The behaviour contrasts sharply with surrounding areas, suggesting that it may signal initial anomalies in the magma or hydrothermal systems. Additionally, this interpretation can be further validated in the lower flank in the future, where a new fumarole emerged around 2005. Changes related to sulphur flows are challenging to observe accurately due to resolution limitations. However, there is promising evidence that the 2019 sulphur flows coincided with an increase in HDI, suggesting the potential for monitoring sulphur flows using satellite technologies in the future. Furthermore, significant HDI increases associated with sulphur flows typically last only one to two years, followed by a return to initial levels. This pattern is likely caused by the erosion and exposure of fresh deposits due to environmental factors such as rainfall, snowmelt, and wind. During the period of sulphur flow movements or before their emergence, significant increases in HDI were observed in the surrounding area, as shown in Figs. 6 and 7. Meanwhile, the HDI values and variations in the sulphur flow areas are similar to those in the surrounding fumarolic deposits, but of smaller magnitude. This could indicate that the liquid sulphur flows are controlled by its source region, as suggested in previous studies at Lastarria Volcano (Naranjo, 1985).

5. Conclusion

In this study, we introduced, tested and applied a remote sensing index called the Hydrothermal Deposit Index (HDI) using the Ultra Blue, Red, SWIR 1, and SWIR 2 bands of multispectral satellite data to facilitate long-term monitoring of hydrothermal deposits. The primary processing tasks were conducted using Google Earth Engine (GEE), a powerful cloud computing platform that provides access to archived historical Landsat 8 and Sentinel 2 multispectral data. Considering the influence of steam plumes and other environmental interferences on volcanic remote sensing, we implemented a median compositing technique to integrate all images captured within each year. This process yielded annual composite images spanning from 2014 to 2023, which were subsequently employed to delineate the distribution of hydrothermal deposits and perform spatiotemporal analysis. Incorporating these composite images, the proposed HDI has been proven effective in accurately delineating hydrothermal deposit zones and visually distinguishing between altered and unaltered materials, surpassing traditional methods.

In the case study of Lastarria Volcano, we identified three distinct hydrothermal deposit zones spanning approximately 600,000 m^2, which closely align with independent data gathered from field surveys

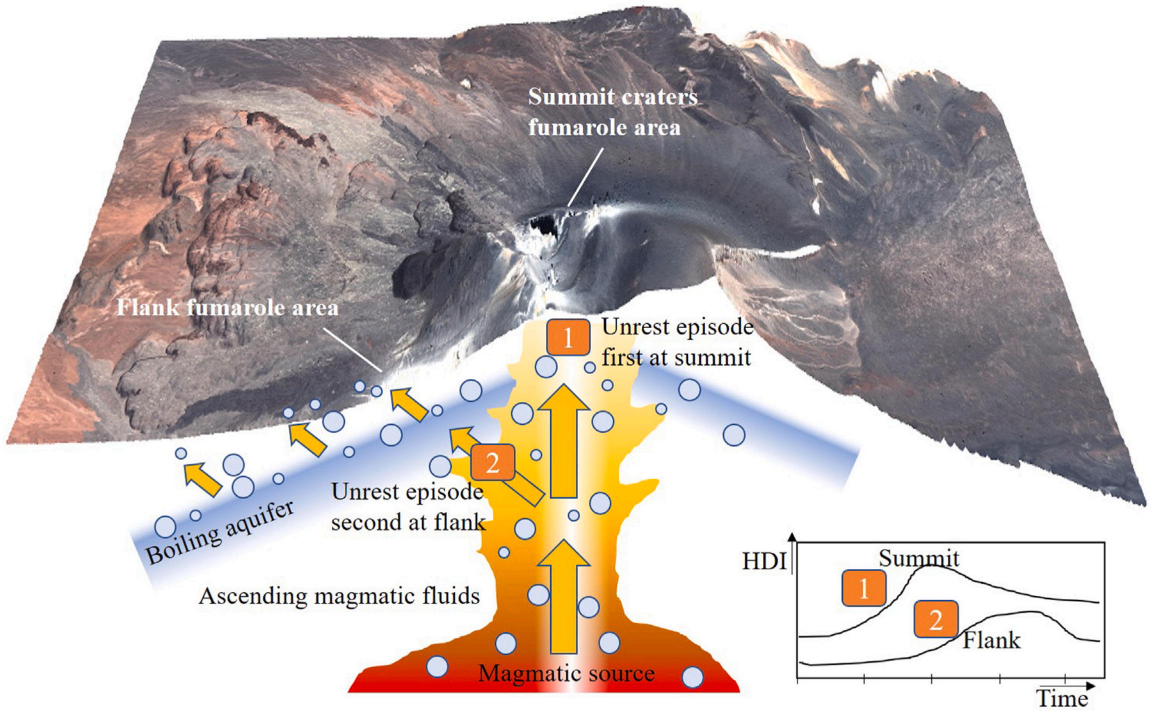

Fig. 11. Conceptual model sketch. The hydrothermal alteration deposit index (HDI) allows monitoring of the surface expressions of activity at Lastarria Volcano (perspective view from SW, vertically 5x exaggerated). Activity at the summit crater fumarole area is compared with that at the flank fumarole area, revealing a time shift in the increase and decrease of activity, which may be linked to the underground pathways of ascending fluids. Conceptual sketch on the ascent path and aquifer contains information from Layana et al. (2023) and Aguilera et al. (2012).

and previous studies. Through time series analysis, we determined periods of both growth and reduction of hydrothermal deposits within the summit crater, alongside the occurrence of sulphur flows in the flank. HDI variations were initially observed within the summit crater and subsequently in the flank. Therefore, we proposed that changes at depth in 2017 drove the migration of hydrothermal fluid from the summit crater to the flank area, and the growth of hydrothermal deposit zones could serve as an early indicator of anomalies in deeper magmatic or hydrothermal systems. In addition, we indicated the emergence of sulphur flows is related to the activity of surrounding fumaroles. In conclusion, this research introduces a robust methodology for extracting hydrothermal deposit information and offers significant insights into the spatiotemporal dynamics and potential hazards associated with hydrothermal activity within volcanic areas. Future research should focus on refining these methodologies to further enhance our understanding of volcanic processes and improve hazard assessments.

CRediT authorship contribution statement

Guosheng Gao: Writing – review & editing, Writing – original draft, Software, Methodology, Formal analysis, Conceptualization. **Thomas R. Walter:** Writing – review & editing, Writing – original draft, Visualization, Validation, Supervision, Methodology, Investigation, Funding acquisition. **Daniel Müller:** Writing – review & editing, Writing – original draft, Validation, Conceptualization. **Pouria Marzban:** Writing – review & editing, Validation, Methodology, Conceptualization. **Simon Plank:** Writing – review & editing, Visualization, Validation, Methodology.

Declaration of competing interest

The authors declare that they have no known competing financial interests or personal relationships that could have appeared to influence the work reported in this paper.

Acknowledgements

G.G. acknowledges financial support from the China Scholarship Council, China (202210710005). This work was supported by ROT-TnROCK, a research project funded by the European Research Council, under the European Union's Horizon Europe Programme [ERC-2023-SyG 101118491], and contributes to the Integrated Plate Boundary Observatory Chile (IPOC) financially supported by GFZ. We thank Felipe Aguilera for discussions on an earlier version of this manuscript. We also extend our thanks to the two anonymous reviewers whose comments improved this work.

Declaration of competing interest

The authors declare that they have no known competing financial interests or personal relationships that could have appeared to influence the work reported in this paper.

Appendix A. Supplementary data

Supplementary material related to this article can be found online at https://doi.org/10.1016/j.geothermics.2025.103255.

Data availability

Data will be made available on request.

References

Abass Saley, A., Baratoux, D., Baratoux, L., Ahoussi, K.E., Yao, K.A., Kouamé, K.J., 2021. Evolution of the Koma Bangou gold panning site (Niger) from 1984 to 2020 using Landsat imagery. Earth Space Sci. 8 (11), e2021EA001879. http://dx.doi.org/10.1038/s42003-021-01817-8.

Africano, F., Bernard, A., 2000. Acid alteration in the fumarolic environment of Usu volcano, Hokkaido, Japan. J. Volcanol. Geotherm. Res. 97 (1), 475–495. http://dx.doi.org/10.1016/S0377-0273(99)00162-6.

AghaKouchak, A., Farahmand, A., Melton, F.S., Teixeira, J., Anderson, M.C., Wardlow, B.D., Hain, C.R., 2015. Remote sensing of drought: Progress, challenges and opportunities. Rev. Geophys. 53 (2), 452–480. http://dx.doi.org/10.1002/2014RG000456.

Aguilera, F., Layana, S., Rodríguez-Díaz, A., González, C., Cortés, J., Inostroza, M., 2016. Hydrothermal alteration, fumarolic deposits and fluids from Lastarria Volcanic Complex: A multidisciplinary study. Andean Geol. 43, 166–196. http://dx.doi.org/10.5027/andgeoV43n2-a02.

Aguilera, F., Tassi, F., Darrah, T., Moune, S., Vaselli, O., 2012. Geochemical model of a magmatic–hydrothermal system at the Lastarria volcano, northern Chile. Bull. Volcanol. 74 (1), 119–134. http://dx.doi.org/10.1007/s00445-011-0489-5.

Azzarini, F.M., Pareschi, M.T., Sbrana, A., Favalli, M., Fulignati, P., 2001. Surface hydrothermal alteration mapping at Vulcano Island using MIVIS data. Int. J. Remote Sens. 22 (11), 2045–2070. http://dx.doi.org/10.1080/01431160118291.

Barrett, T.J., MacLean, W.H., 1997. Volcanic sequences, lithogeochemistry, and hydrothermal alteration in some bimodal volcanic-associated massive sulfide systems. In: Volcanic Associated Massive Sulfide Deposits: Processes and Examples in Modern and Ancient Settings. Society of Economic Geologists, ISBN: 9781629490151, http://dx.doi.org/10.5382/Rev.08.05.

Bian, J., Li, A., Lei, G., Zhang, Z., Nan, X., 2020. Global high-resolution mountain green cover index mapping based on Landsat images and Google Earth Engine. ISPRS J. Photogramm. Remote Sens. 162, 63–76. http://dx.doi.org/10.1016/j.isprsjprs.2020.02.011.

Blickensdörfer, L., Schwieder, M., Pflugmacher, D., Nendel, C., Erasmi, S., Hostert, P., 2022. Mapping of crop types and crop sequences with combined time series of Sentinel-1, Sentinel-2 and Landsat 8 data for Germany. Remote Sens. Environ. 269, 112831. http://dx.doi.org/10.1016/j.rse.2021.112831.

Carlson, T.N., Ripley, D.A., 1997. On the relation between NDVI, fractional vegetation cover, and leaf area index. Remote Sens. Environ. 62 (3), 241–252. http://dx.doi.org/10.1016/S0034-4257(97)00104-1.

Carrasco, L., O'Neil, A.W., Morton, R.D., Rowland, C.S., 2019. Evaluating combinations of temporally aggregated Sentinel-1, Sentinel-2 and Landsat 8 for land cover mapping with google earth engine. Remote Sens. 11 (3), 288. http://dx.doi.org/10.3390/rs11030288.

Carrino, T.A., Crósta, A.P., Toledo, C.L.B., Silva, A.M., Silva, J.L., 2015. Geology and hydrothermal alteration of the Chapi Chiara prospect and nearby targets, Southern Peru, using ASTER data and reflectance spectroscopy. Econ. Geol. 110 (1), 73–90. http://dx.doi.org/10.2113/econgeo.110.1.73.

Chabrillat, S., Gholizadeh, A., Neumann, C., Berger, D., Milewski, R., Ogen, Y., Ben-Dor, E., 2019. Preparing a soil spectral library using the Internal Soil Standard (ISS) method: Influence of extreme different humidity laboratory conditions. Geoderma 355, 113855. http://dx.doi.org/10.1016/j.geoderma.2019.07.013.

Crósta, A.P., Moore, J.M., 1989. Geological mapping using Landsat Thematic Mapper imagery in Almeria Province, south-east Spain. Mining Geol. 10 (3), 505–514. http://dx.doi.org/10.1080/01431168908903888.

Darmawan, H., Troll, V.R., Walter, T.R., Deegan, F.M., Geiger, H., Heap, M.J., Seraphine, N., Harris, C., Humaida, H., Müller, D., 2022. Hidden mechanical weaknesses within lava domes provided by buried high-porosity hydrothermal alteration zones. Sci. Rep. 12 (1), 3202. http://dx.doi.org/10.1038/s41598-022-06765-9.

Defries, R.S., Townshend, J.R.G., 1994. NDVI-derived land cover classifications at a global scale. Int. J. Remote Sens. 15 (17), 3567–3586. http://dx.doi.org/10.1080/01431169408954345.

Di Tommaso, I., Rubinstein, N., 2007. Hydrothermal alteration mapping using ASTER data in the Infiernillo porphyry deposit, Argentina. Ore Geol. Rev. 32 (1), 275–290. http://dx.doi.org/10.1016/j.oregeorev.2006.05.004.

Froger, J.-L., Remy, D., Bonvalot, S., Legrand, D., 2007. Two scales of inflation at Lastarria-Cordon del Azufre volcanic complex, central Andes, revealed from ASAR-ENVISAT interferometric data. Earth Planet. Sci. Lett. 255 (1), 148–163. http://dx.doi.org/10.1016/j.epsl.2006.12.012.

Frutuoso, R., Lima, A., Teodoro, A.C., 2021. Application of remote sensing data in gold exploration: Targeting hydrothermal alteration using Landsat 8 imagery in northern Portugal. Arab. J. Geosci. 14 (6), 459. http://dx.doi.org/10.1007/s12517-021-06786-0.

García-Soto, A.Y., Pandarinath, K., Santoyo, E., Gonzalez-Partida, E., 2024. Hydrothermal alteration of the surface volcanic rocks at the Acoculco geothermal field, Mexico: A multi-parametric approach. Acta Geochim. http://dx.doi.org/10.1007/s11631-024-00683-5.

Gersman, R., Ben-Dor, E., Beyth, M., Avigad, D., Abraha, M., Kibreab, A., 2008. Mapping of hydrothermally altered rocks by the EO-1 Hyperion sensor, Northern Danakil Depression, Eritrea. Int. J. Remote Sens. 29 (13), 3911–3936. http://dx.doi.org/10.1080/01431160701874587.

Gorelick, N., Hancher, M., Dixon, M., Ilyushchenko, S., Thau, D., Moore, R., 2017. Google Earth Engine: Planetary-scale geospatial analysis for everyone. Remote Sens. Environ. 202, 18–27. http://dx.doi.org/10.1016/j.rse.2017.06.031.

Hafeez, S., Wong, M.S., Abbas, S., Asim, M., 2022. Evaluating Landsat-8 and Sentinel-2 data consistency for high spatiotemporal inland and coastal water quality monitoring. Remote Sens. 14 (13), 3155. http://dx.doi.org/10.3390/rs14133155.

Heap, M.J., Baumann, T., Gilg, H.A., Kolzenburg, S., Ryan, A.G., Villeneuve, M., Russell, J.K., Kennedy, L.A., Rosas-Carbajal, M., Clynne, M.A., 2021. Hydrothermal alteration can result in pore pressurization and volcano instability. Geology 49 (11), 1348–1352. http://dx.doi.org/10.1130/G49063.1.

Heap, M.J., Troll, V.R., Kushnir, A.R.L., Gilg, H.A., Collinson, A.S.D., Deegan, F.M., Darmawan, H., Seraphine, N., Neuberg, J., Walter, T.R., 2019. Hydrothermal alteration of andesitic lava domes can lead to explosive volcanic behaviour. Nat. Commun. 10 (1), 5063. http://dx.doi.org/10.1038/s41467-019-13102-8.

Henderson, S.T., Delgado, F., Elliott, J., Pritchard, M.E., Lundgren, P.R., 2017. Decelerating uplift at Lazufre volcanic center, Central Andes, from A.D. 2010 to 2016, and implications for geodetic models. Geosphere 13 (5), 1489–1505. http://dx.doi.org/10.1130/GES01441.1.

Hird, J.N., DeLancey, E.R., McDermid, G.J., Kariyeva, J., 2017. Google earth engine, open-access satellite data, and machine learning in support of large-area probabilistic wetland mapping. Remote Sens. 9 (12), 1315. http://dx.doi.org/10.3390/rs9121315.

Inostroza, M., Fernandez, B., Aguilera, F., Layana, S., Walter, T.R., Zimmer, M., Rodríguez-Díaz, A., Oelze, M., 2023. Physical and chemical characteristics of active sulfur flows observed at Lastarria volcano (northern Chile) in January 2019. Front. Earth Sci. 11, http://dx.doi.org/10.3389/feart.2023.1197363.

Ishikawa, Y., SAWAGUCHI, T., IWAYA, S., HORIUCHI, M., 1976. Delineation of prospecting targets for Kuroko deposits based on modes of volcanism of underlying dacite and alteration haloes. Mining Geol. 26 (136), 105–117. http://dx.doi.org/10.11456/shigenchishitsu1951.26.105.

Izawa, M.R.M., Cloutis, E.A., Rhind, T., Mertzman, S.A., Applin, D.M., Stromberg, J.M., Sherman, D.M., 2019. Spectral reflectance properties of magnetites: Implications for remote sensing. Icarus 319, 525–539. http://dx.doi.org/10.1016/j.icarus.2018.10.002.

Jakobsson, S.P., Moore, J.G., 1986. Hydrothermal minerals and alteration rates at Surtsey volcano, Iceland. Geol. Soc. Am. Bull. 97 (5), 648. http://dx.doi.org/10.1130/0016-7606(1986)97<648:HMAARA>2.0.CO;2.

John, D.A., Sisson, T.W., Breit, G.N., Rye, R.O., Vallance, J.W., 2008. Characteristics, extent and origin of hydrothermal alteration at Mount Rainier Volcano, Cascades Arc, USA: Implications for debris-flow hazards and mineral deposits. J. Volcanol. Geotherm. Res. 175 (3), 289–314. http://dx.doi.org/10.1016/j.jvolgeores.2008.04.004.

Kereszturi, G., Heap, M., Schaefer, L.N., Darmawan, H., Deegan, F.M., Kennedy, B., Komorowski, J.-C., Mead, S., Rosas-Carbajal, M., Ryan, A., Troll, V.R., Villeneuve, M., Walter, T.R., 2023. Porosity, strength, and alteration – Towards a new volcano stability assessment tool using VNIR-SWIR reflectance spectroscopy. Earth Planet. Sci. Lett. 602, 117929. http://dx.doi.org/10.1016/j.epsl.2022.117929.

Kereszturi, G., Schaefer, L.N., Miller, C., Mead, S., 2020. Hydrothermal alteration on composite volcanoes: Mineralogy, hyperspectral imaging, and aeromagnetic study of Mt Ruapehu, New Zealand. Geochem. Geophys. Geosyst. 21 (9), e2020GC009270. http://dx.doi.org/10.1029/2020GC009270.

Kereszturi, G., Schaefer, L.N., Schleiffarth, W.K., Procter, J., Pullanagari, R.R., Mead, S., Kennedy, B., 2018. Integrating airborne hyperspectral imagery and LiDAR for volcano mapping and monitoring through image classification. Int. J. Appl. Earth Obs. Geoinf. 73, 323–339. http://dx.doi.org/10.1016/j.jag.2018.07.006.

Layana, S., Aguilera, F., Inostroza, M., Tassi, F., Wilkes, T.C., Bredemeyer, S., González, C., Pering, T.D., McGonigle, A.J.S., 2023. Evolution of the magmatic-hydrothermal system at Lastarria volcano (Northern Chile) between 2006 and 2019: Insights from fluid geochemistry. Front. Earth Sci. 11, http://dx.doi.org/10.3389/feart.2023.1114001.

Lechler, P., Desilets, M., 1987. A review of the use of loss on ignition as a measurement of total volatiles in whole-rock analysis. Chem. Geol. 63 (3-4), 341–344. http://dx.doi.org/10.1016/0009-2541(87)90171-9.

Li, S., Xu, L., Jing, Y., Yin, H., Li, X., Guan, X., 2021. High-quality vegetation index product generation: A review of NDVI time series reconstruction techniques. Int. J. Appl. Earth Obs. Geoinf. 105, 102640. http://dx.doi.org/10.1016/j.jag.2021.102640.

Lopez, T., Aguilera, F., Tassi, F., De Moor, J.M., Bobrowski, N., Aiuppa, A., Tamburello, G., Rizzo, A.L., Liuzzo, M., Viveiros, F., Cardellini, C., Silva, C., Fischer, T., Jean-Baptiste, P., Kazayaha, R., Hidalgo, S., Malowany, K., Lucic, G., Bagnato, E., Chiodini, G., 2018. New insights into the magmatic-hydrothermal system and volatile budget of Lastarria volcano, Chile: Integrated results from the 2014 IAVCEI CCVG 12th Volcanic Gas Workshop. Geosphere 14 (3), 983–1007. http://dx.doi.org/10.1130/GES01495.1.

Martínez, B., Gilabert, M.A., 2009. Vegetation dynamics from NDVI time series analysis using the wavelet transform. Remote Sens. Environ. 113 (9), 1823–1842. http://dx.doi.org/10.1080/01431168708948645.

Marzban, P., Bredemeyer, S., Walter, T.R., Kästner, F., Müller, D., Chabrillat, S., 2023. Hydrothermally altered deposits of 2014 Askja landslide, Iceland, identified by remote sensing imaging. Front. Earth Sci. 11, http://dx.doi.org/10.3389/feart.2023.1083043.

Masek, J.G., Wulder, M.A., Markham, B., McCorkel, J., Crawford, C.J., Storey, J., Jenstrom, D.T., 2020. Landsat 9: Empowering open science and applications through continuity. Remote Sens. Environ. 248, 111968. http://dx.doi.org/10.1016/j.rse.2020.111968.

Massimetti, F., Coppola, D., Laiolo, M., Valade, S., Cigolini, C., Ripepe, M., 2020. Volcanic hot-spot detection using SENTINEL-2: A comparison with MODIS–MIROVA thermal data series. Remote Sens. 12 (5), 820. http://dx.doi.org/10.3390/rs12050820.

Mathieu, L., 2018. Quantifying hydrothermal alteration: A review of methods. Geosciences 8 (7), 245. http://dx.doi.org/10.3390/geosciences8070245.

Mia, B., Fujimitsu, Y., 2012. Mapping hydrothermal altered mineral deposits using Landsat 7 ETM+ image in and around Kuju volcano, Kyushu, Japan. J. Earth Syst. Sci. 121, 1049–1057. http://dx.doi.org/10.1007/s12040-012-0211-9.

Mia, M.B., Fujimitsu, Y., Nishijima, J., 2019. Exploration of hydrothermal alteration and monitoring of thermal activity using multi-source satellite images: A case study of the recently active Kirishima volcano complex on Kyushu Island, Japan. Geothermics 79, 26–45. http://dx.doi.org/10.1016/j.geothermics.2019.01.006.

Montanaro, C., Mick, E., Salas-Navarro, J., Caudron, C., Cronin, S.J., de Moor, J.M., Scheu, B., Stix, J., Strehlow, K., 2022. Phreatic and hydrothermal eruptions: from overlooked to looking over. Bull. Volcanol. 84 (6), 64. http://dx.doi.org/10.1007/s00445-022-01571-7.

Müller, D., Bredemeyer, S., Zorn, E., De Paolo, E., Walter, T.R., 2021. Surveying fumarole sites and hydrothermal alteration by unoccupied aircraft systems (UAS) at the La Fossa cone, Vulcano Island (Italy). J. Volcanol. Geotherm. Res. 413, 107208. http://dx.doi.org/10.1016/j.jvolgeores.2021.107208.

Myneni, R.B., Keeling, C.D., Tucker, C.J., Asrar, G.R., Nemani, R.R., 1997. Increased plant growth in the northern high latitudes from 1981 to 1991. Nature 386, 698–702. http://dx.doi.org/10.1038/386698a0.

Naranjo, J.A., 1985. Sulphur flows at Lastarria volcano in the North Chilean Andes. Nature 313, 778. http://dx.doi.org/10.1038/313778a0.

Nesbitt, H., Young, G.M., 1982. Early Proterozoic climates and plate motions inferred from major element chemistry of lutites. Nature 299 (5885), 715–717. http://dx.doi.org/10.1038/299715a0.

Okujeni, A., Kowalski, K., Lewińska, K.E., Schneidereit, S., Hostert, P., 2024. Multidecadal grassland fractional cover time series retrieval for Germany from the Landsat and Sentinel-2 archives. Remote Sens. Environ. 302, 113980. http://dx.doi.org/10.1016/j.rse.2023.113980.

Olmanson, L.G., Brezonik, P.L., Finlay, J.C., Bauer, M.E., 2016. Comparison of Landsat 8 and Landsat 7 for regional measurements of CDOM and water clarity in lakes. Remote Sens. Environ. 185, 119–128. http://dx.doi.org/10.1016/j.rse.2016.01.007.

Parker, A., 1970. An index of weathering for silicate rocks. Geol. Magazine 107 (6), 501–504. http://dx.doi.org/10.1017/S0016756800058581.

Plank, S., Marchese, F., Genzano, N., Nolde, M., Martinis, S., 2020. The short life of the volcanic island New Late'iki (Tonga) analyzed by multi-sensor remote sensing data. Sci. Rep. 10 (1), 22293. http://dx.doi.org/10.1038/s41598-020-79261-7.

Pour, A.B., Hashim, M., van Genderen, J., 2013. Detection of hydrothermal alteration zones in a tropical region using satellite remote sensing data: Bau goldfield, Sarawak, Malaysia. Ore Geol. Rev. 54, 181–196. http://dx.doi.org/10.1016/j.oregeorev.2013.03.010.

Pritchard, M.E., Simons, M., 2002. A satellite geodetic survey of large-scale deformation of volcanic centres in the central Andes. Nature 418, 168–171. http://dx.doi.org/10.1038/nature00872.

Ranjbar, H., Honarmand, M., Moezifar, Z., 2004. Application of the Crosta technique for porphyry copper alteration mapping, using ETM+ data in the southern part of the Iranian volcanic sedimentary belt. J. Asian Earth Sci. 24 (2), 237–243. http://dx.doi.org/10.1016/j.jseaes.2003.11.001.

Rodríguez, A., van Bergen, M.J., 2017. Superficial alteration mineralogy in active volcanic systems: An example of Poás volcano, Costa Rica. J. Volcanol. Geotherm. Res. 346, 54–80. http://dx.doi.org/10.1016/j.jvolgeores.2017.04.006.

Roy, D.P., Huang, H., Boschetti, L., Giglio, L., Yan, L., Zhang, H.H., Li, Z., 2019. Landsat-8 and Sentinel-2 burned area mapping—A combined sensor multi-temporal change detection approach. Remote Sens. Environ. 231, 111254. http://dx.doi.org/10.1016/j.rse.2019.111254.

Ruch, J., Manconi, A., Zeni, G., Solaro, G., Pepe, A., Shirzaei, M., Walter, T.R., Lanari, R., 2009. Stress transfer in the Lazufre volcanic area, central Andes. Geophys. Res. Lett. 36 (22), http://dx.doi.org/10.1029/2009GL041276.

Sabins, F.F., 1999. Remote sensing for mineral exploration. Ore Geol. Rev. 14 (3–4), 157–183. http://dx.doi.org/10.1016/S0169-1368(99)00007-4.

Salaün, A., Villemant, B., Gérard, M., Komorowski, J.-C., Michel, A., 2011. Hydrothermal alteration in andesitic volcanoes: Trace element redistribution in active and ancient hydrothermal systems of Guadeloupe (Lesser Antilles). J. Geochem. Explor. 111 (3), 59–83. http://dx.doi.org/10.1016/j.gexplo.2011.06.004.

Schaefer, L.N., Kereszturi, G., Kennedy, B.M., Villeneuve, M., 2023. Characterizing lithological, weathering, and hydrothermal alteration influences on volcanic rock properties via spectroscopy and laboratory testing: A case study of Mount Ruapehu volcano, New Zealand. Bull. Volcanol. 85 (8), 43. http://dx.doi.org/10.1007/s00445-023-01657-w.

Schwartz, G.M., 1959. Hydrothermal alteration. Econ. Geol. 54 (2), 161–183. http://dx.doi.org/10.2113/gsecongeo.54.2.161.

Sengar, V.K., Venkatesh, A.S., Champati Ray, P.K., Sahoo, P.R., Khan, I., Chattoraj, S.L., 2020. Spaceborne mapping of hydrothermal alteration zones associated with the Mundiyawas-Khera copper deposit, Rajasthan, India, using SWIR bands of ASTER: Implications for exploration targeting. Ore Geol. Rev. 118, 103327. http://dx.doi.org/10.1016/j.oregeorev.2020.103327.

Shebl, A., Abdellatif, M., Badawi, M., Dawoud, M., Fahil, A.S., Csámer, Á., 2023. Towards better delineation of hydrothermal alterations via multi-sensor remote sensing and airborne geophysical data. Sci. Rep. 13 (1), 7406. http://dx.doi.org/10.1038/s41598-023-34531-y.

Shevchenko, A.V., Walter, T.R., Gudmundsson, M.T., Belart, J.M., Marzban, P., Zorn, E.U., Sæmundsson, Þ., Helgason, J.K., Turowski, J.M., Vassileva, M.S., et al., 2024. Morphological changes of the south-eastern wall of Askja caldera, Iceland over the past 80 years. Commun. Earth & Environ. 5 (1), 441. http://dx.doi.org/10.1038/s43247-024-01616-z.

Spica, Z., Legrand, D., Iglesias, A., Walter, T.R., Heimann, S., Dahm, T., Froger, J.-L., Rémy, D., Bonvalot, S., West, M., Pardo, M., 2015. Hydrothermal and magmatic reservoirs at Lazufre volcanic area, revealed by a high-resolution seismic noise tomography. Earth Planet. Sci. Lett. 421, 27–38. http://dx.doi.org/10.1016/j.epsl.2015.03.042.

Sun, Y., Tian, S., Di, B., 2017. Extracting mineral alteration information using WorldView-3 data. Geosci. Front. 8 (5), 1051–1062. http://dx.doi.org/10.1016/j.gsf.2016.10.008.

Thomas, I.L., Ching, N.P., Benning, V.M., D'Aguanno, J.A., 1987. Review Article a review of multi-channel indices of class separability. Int. J. Remote Sens. 8 (3), 331–350. http://dx.doi.org/10.1080/01431168708948645.

Walter, T.R., Zorn, E.U., Harnett, C.E., Shevchenko, A.V., Belousov, A., Belousova, M., Vassileva, M.S., 2022. Influence of conduit and topography complexity on spine extrusion at Shiveluch volcano, Kamchatka. Commun. Earth & Environ. 3 (1), 169. http://dx.doi.org/10.1038/s43247-022-00491-w.

Zeng, C., Shen, H., Zhang, L., 2013. Recovering missing pixels for Landsat ETM+ SLC-off imagery using multi-temporal regression analysis and a regularization method. Remote Sens. Environ. 131, 182–194. http://dx.doi.org/10.1016/j.rse.2012.12.012.

Zhu, Z., Woodcock, C.E., 2014. Automated cloud, cloud shadow, and snow detection in multitemporal Landsat data: An algorithm designed specifically for monitoring land cover change. Remote Sens. Environ. 152, 217–234. http://dx.doi.org/10.1016/j.rse.2014.06.012.